New Evidence for the Role of Emerging Flux in a Solar Filament's Slow Rise Preceding Its CME-producing Fast Eruption — **Source link** ↗

Alphonse C. Sterling, Louise K. Harra, Ronald L. Moore

Institutions: Marshall Space Flight Center, University College London

Topics: Protein filament, Coronal mass ejection, Solar flare and Solar prominence

Related papers:

- Onset of the Magnetic Explosion in Solar Flares and Coronal Mass Ejections

- The Atmospheric Imaging Assembly (AIA) on the Solar Dynamics Observatory (SDO)

- A Model for Solar Coronal Mass Ejections

- Confined and Ejective Eruptions of Kink-unstable Flux Ropes

- The Torus instability

New Evidence for the Role of Emerging Flux in a Solar Filament's Slow Rise Preceding its CME-Producing Fast Eruption

Alphonse C. Sterling[1]

NASA/Marshall Space Flight Center, VP62/Space Science Office, Huntsville, AL 35805

alphonse.sterling@nasa.gov

Louise K. Harra

UCL-Mullard Space Science Laboratory, Holmbury St Mary, Dorking, Surrey RH5 6NT, UK

lkh@mssl.ucl.ac.uk

and

Ronald L. Moore

NASA/Marshall Space Flight Center, VP62/Space Science Office, Huntsville, AL 35805

ron.moore@nasa.gov

---

[1]Current address: JAXA/Institute of Space and Astronautical Science, Hinode Group, 3-1-1 Yoshinodai, Sagamihara, Kanagawa 229-8510, Japan

ABSTRACT

We observe the eruption of a large-scale ($\approx$ 300,000 km) quiet-region solar filament, leading to an Earth-directed "halo" coronal mass ejection (CME). We use coronal imaging data in EUV from the EUV Imaging Telescope (EIT) on the Solar and Heliospheric Observatory (SOHO) satellite, and in soft X-rays (SXRs) from the Soft X-ray Telescope (SXT) on the Yohkoh satellite. We also use spectroscopic data from the Coronal Diagnostic Spectrometer (CDS), magnetic data from the Michelson Doppler Imager (MDI), and white-light coronal data from the Large Angle and Spectrometric Coronagraph Experiment (LASCO), all on SOHO. Initially the filament shows a slow ($\sim$ 1 km s^{-1} projected against the solar disk) and approximately constant-velocity rise for about 6 hours, before erupting rapidly, reaching a velocity of $\sim$ 8 km s^{-1} over the next $\approx$ 25 min. CDS Doppler data show Earth-directed filament velocities ranging from $<$ 20 km s^{-1} (the noise limit) during the slow-rise phase, to $\sim$ 100 km s^{-1} early in the eruption. Beginning within 10 hours prior to the start of the slow rise, localized new magnetic flux emerged near one end of the filament. Near the start of and during the slow-rise phase, SXR microflaring occurred repeatedly at the flux-emergence site, in conjunction with the development of a fan of SXR illumination of the magnetic arcade over the filament. The SXR microflares, development of the SXR fan, and motion of the slow-rising filament are all consistent with "tether-weakening" reconnection occurring between the newly-emerging flux and the overlying arcade field containing the filament field. The microflares and fan structure are not prominent in EUV, and would not have been detected without the SXR data. Standard "twin dimmings" occur near the location of the filament, and "remote dimmings" and "brightenings" occur further removed from the filament. We interpret these intensity changes to be reasonable signatures of the expan-

sion ("opening") of the erupting field and its reconnection with overarching field during the eruption. We cannot discern whether the transition from the slow rise to the fast eruption was caused by a final episode of tether-weakening reconnection or by one or some combination of other possible mechanisms allowed by the observations, including tether-cutting reconnection, breakout reconnection, and MHD instability or loss of magnetostatic equilibrium. In contrast, the observations strongly favor tether-weakening reconnection as the cause of the slow rise prior to the transition to fast eruption.

Subject headings: Sun: flares — Sun: filaments — Sun: UV radiation — Sun: X-rays, gamma rays — Sun: coronal mass ejections (CMEs)

1. Introduction

Solar eruptions result in the rapid expulsion from the Sun of magnetic field, material, and radiations in the form of coronal mass ejections (CMEs) and solar flares. Why eruptions occur is a major outstanding question of solar physics. Research over the past several decades, and in particular that based on observations from space over the last three decades, has vastly improved our understanding of these events, and led to formation of several ideas for the eruption mechanism.

We know that eruptions occur at locations on the Sun where there is a build-up of a large amount of magnetic energy, and eruptions occur when this energy is released via some process. Many of the eruption models deal with how this energy release is accomplished. For example, Forbes & Isenberg (1991) and Lin et al. (1998) discuss how convergence of magnetic flux below a flux tube situated a magnetic-polarity inversion line can lead to enhancement of the flux tube and its eventual disruption due to an instability. Chen & Shibata (2000) present a model where eruption results when tension in a sheared arcade or flux rope field is weakened via reconnection between that main field and an emerging flux; this is similar to the tether weakening and tether cutting schemes presented by Moore & Roumeliotis (1992) and by Moore & LaBonte (1980); Sturrock (1989); Moore & Roumeliotis (1992); Moore et al. (2001). Antiochos (1998) and Antiochos, DeVore, & Klimchuk (1999) discuss instead disruption of a sheared core field from above, when tension between the core field and an overlying restraining field (of polarity opposite that of the core field) is reduced via reconnection between the two field systems. Another theoretical possibility for the eruption cause is kinking (kink instability) of an emerging flux rope (e.g., Sturrock et al. 2001; Linker et al. 2001; Fan & Gibson 2004; Rust & LaBonte 2005; Gibson & Fan 2006). Some reviews describing basic aspects of several eruption ideas are Forbes (2000), Klimchuk (2001), Lin, Soon, & Baliunas (2003), and Moore & Sterling (2006).

To determine which (if any) of these mechanisms is predominately responsible for eruptions, it is necessary to observe the evolution of eruptions and compare with expectations from the models. In particular, we would like to know the behavior of the magnetic field around the core of the erupting region prior to and during the explosive eruption. We have been attempting to study this for several events through detailed analysis using filaments as tracers of the the otherwise-invisible evolving field, and for some of these also examining intensity variations (dimmings and brightenings) in EUV and soft X-rays (SXR) that can be indicative of evolution of the field outside of the filament (Sterling & Moore 2003, 2004a,b, 2005). The purpose of the present paper is to continue these investigations by studying an eruption that occurred near solar disk center on 2001 February 28. Similar to the previous eruptions we have reported on, this eruption also involves a filament whose early movement is a slow rise (as often occurs, e.g. Tandberg-Hanssen, Martin, & Hansen 1980; Kahler et al. 1988; Feynman & Ruzmaikin 2004), indicative of a slow pre-eruption expansion of the magnetic fields involved in the eruption. We also investigate spectroscopic Doppler motions of the filament and associated features from around the time of eruption onset for this event. We will show that for this event there is strong evidence that the cause of the slow rise of the filament was magnetic reconnection between the main filament field and newly-emerging flux, but we could not isolate a single cause of the onset of the rapid eruption (similar to the collective results of several of our previous investigations, Moore & Sterling 2006).

This eruption occurred in a quiet region, and therefore the evolution toward eruption was relatively slow compared to typical active region eruptions; this is a consequence of the relatively weak field strength in quiet regions, and correspondingly lower Alfvén velocities. Because of this slow evolution, we are able to follow closely the timings of filament motions compared with various intensity changes, even with the relatively low or non-uniform cadence of our observations.

2. Instrumentation and Data

We use imaging, magnetic, and spectroscopic data for our analysis. Imaging data include those in EUV from the EUV Imaging Telescope (EIT; Delaboudinière et al. 1995) on the Solar and Heliospheric Observatory (SOHO) satellite, and in SXRs from the soft X-ray telescope (SXT; Tsuneta et al. 1991) on the Yohkoh satellite. Magnetic data are from the Michelson Doppler Imager (MDI; Scherrer et al. 1995) and spectroscopic data, including rastered images, are from the Coronal Diagnostic Spectrometer (CDS; Harrison et al. 1995), both on SOHO.

Our EIT data are primarily from its 195 Å Fe XII filter at a 12-minute cadence and spatial pixel resolution of $2''.6$. EIT's full-disk coverage is ideal for observing larger-scale eruptions, such as the one we study here. We use mainly full-disk AlMg-filter images from SXT, with cadence varying from about 2 minutes, to over an hour during times of spacecraft night or data gaps. Filaments are visible in the EUV images (e.g., Mein et al. 2001; Schmieder et al. 2004; Anzer & Heinzel 2005), and we use these images to track the filament movements.

CDS provides spectral information in various lines, and for this study we generally used O V data. CDS has a slit length of $240''$, and a spatial resolution of $4.06'' \times 1.68''$. We used CDS images generated by rastering across an area of the Sun from west to east (right to left in the images). Each raster consisted of 260 steps and took ≈ 10 min, and so that is the cadence of our CDS raster images. For the current set of observations the CDS field of view (FOV) was $250'' \times 160''$, and it was in a mode where the rastering occurred repeatedly over the same fixed heliocentric location, with solar features rotating with time into its FOV from the east and out of its FOV in the west. In computing velocities in the region of the filament eruption, we took zero velocity to be the average of the rasters before the filament appeared in the CDS field of view. Hence the Doppler velocities measured

are relative to the quiet background velocity, which is the most accurate way to deal with this issue. The data were calibrated using the standard CDS software which corrects for geometrical distortions as well as the standard instrumental corrections.

The eruption occurred on 2001 February 28, beginning near 12:00 UT, with the filament that erupted located at longitude between about 5° and 15° west of Sun center and latitude between 5° N and 20° S. It occurred in a weak magnetic region, with only small spots present. Evolution toward eruption was relatively slow, with a slow-rise pre-eruption phase lasting several hours (compared to typically only a few minutes for strong-field active-region eruptions) and the SXR output relatively weak; SXR flux from the 1—8 Å channel of the *GOES* satellite showed a weak increase above background to the mid-B level near 13:30 UT that likely resulted from this eruption, and several even weaker increases at earlier times that may have been from imaged SXR enhancements that we observed during the pre-eruption phase (cf. Fig. 5 below). White-light coronal images from the Large Angle and Spectrometric Coronagraph Experiment (LASCO; Brueckner et al. 1995) on *SOHO* recorded a partial halo CME from 14:50 UT, with a possible precursor visible from as early as 13:50 UT (Fig. 1). Its projected velocity against the plane of the sky was ≈ 300 km s^{-1}, according to the LASCO CME catalog (Yashiro et al. 2004).

3. Observations and Analysis

3.1. Filament Motions

Figure 2 shows EIT images of the erupting region, where arrows point out the filament. Prior to eruption the filament undergoes slow movement beginning about 6 hours prior to eruption; it shows substantial change between Figures 2a and 2b, particularly the southern portion of the filament (compare the two southernmost arrows in the two panels). By

the time of Figure 2c, the filament has erupted, with a bright flare loop visible in box 5 and regions around boxes 2 and 3 having undergone intensity dimming compared to the previous panel. Figure 2d shows the situation several hours after eruption, where additional dimmings have occurred in boxes 6 and 7. Video 1 is an EIT movie of the erupting filament.

Figure 3a (and also Fig. 5a) shows the movement of the filament along the fiducials of Figure 2a. Our error bars are 1σ uncertainties based on three independent measurements of the filament motion. Some of the motions prior to 6:00 UT may be real, indicating that filament is undulating prior to eruption, perhaps due to unresolved counterstreaming or twist (e.g., Wiik et al. 1997). At about 5:30 UT the filament begins moving out along the southern fiducial. This motion continues until about 11:30 UT, after which time the filament rapidly accelerates and erupts. Thus, for about 6 hours the filament undergoes a slow-rise phase prior to eruption, similar to what we have seen in earlier studies. Motion along the northern fiducial of Figure 2 becomes unambiguously pronounced after about 11:00 UT, although more subtle motions of the filament are apparent at earlier times (see video 1), and these are reflected in the plot in Figure 3a. Motions of the northern portion of the filament are less obvious than in its southern portion perhaps because the motions are directed along the line of sight, or because this portion of the filament is more stationary than the southern portion during the slow rise. Figure 3a shows the north filament's curve apparently decreasing in height with time; actually it is merely moving in a direction opposite to that of the southern portion of the filament. It is difficult to detect the northern portion of the filament at the time of eruption in the EIT images (just past 12:00 UT), and so the curve in the plot just terminates.

From Figure 3a we can measure the velocity of the filament. If we take the motion during the slow-rise phase to be constant, a least-square fit between 07:24:57 UT and 11:11:30 UT gives a speed of 0.8 km s^{-1} for the slow rise along the southern fiducial. After

eruption starts a linear fit does not seem appropriate for a very extended time period. Between 11:35:32 UT and 12:47:33 UT the motion is roughly linear, and a linear fit gives a speed of about 7.5 km s^{-1}. These values are for motion projected against the disk; as the eruption is near disk center and appears to be roughly vertical, the radial velocity away the Sun will be substantially larger. We can estimate the outward velocity for the southern fiducial, assuming vertical motions. At the time of eruption the filament along that fiducial was between about 8° and 12° away from disk center. This gives the radial velocities to be between about 5 and 7 times the projected values; that is, the slow rise velocity is 5 ± 1 km s^{-1}, and early in the eruption the velocity is 45 ± 8 km s^{-1}. Motions of the filament projected on the disk along the northern fiducial is initially to the east, opposite that of the southern part of the filament. This indicates that as the filament erupts it either twists as it rises, or it expands and appears to twist because different portions of it move toward opposite sides of the line-of-sight between the Sun and the *SOHO* satellite.

3.2.   Intensity Variations During Slow-Rise Phase and Eruption

Figure 3b shows the EIT intensities as functions of time (lightcurves) integrated over the boxes of Figure 2. For context, we first discuss boxes 5 and 10. Box 5 is at the location of the main flaring loops, and its lightcurve shows that the primary flare starts in EUV near 13:00 UT. Weaker brightenings are discernable at earlier times at and around the box 5 location, and these brightenings are reflected in some of the fluctuations in the box 5 lightcurve from at least 10:00 UT. Box 1 is of a region that shows substantial low-level activity during the event; this is one of our most important boxes since, as we shall discuss in §4, activity at this location could have played a primary role in the initiation of the eruption of the filament and CME. Boxes 2 and 3 are locations of a pair of dimmings ("twin dimmings," §3.3) that form on either end of the flare arcade. Boxes 6, 7, and 9

are at regions where we have identified dimmings that are farther removed from the main erupting region than those of boxes 2 and 3 ("remote dimmings," §3.3). Box 8 is a location where we also see intensity changes, but primarily in SXRs.

Figure 4 shows AlMg-filter SXR images from SXT of the same region as that in Figure 2. Loops in the region prior to eruption are consistent with a sheared magnetic geometry, with a roughly sigmoid shape (Sterling & Hudson 1997; Canfield, Hudson, & McKenzie 1999). The filament is not visible in the SXR images, but arrows in Figure 4b point out a bright SXR loop; this is the last loop of a fan of loops that shows up prominently in the SXR images from about the time of the start of the filament's slow-rise phase (cf. Fig. 3a), and persists until the time of eruption, as we will discuss in §4. This SXR feature has no obvious significant manifestation in the EUV images.

Figure 5 is analogous to Figure 3, but for SXRs instead of EUV. As in Figure 3, the box 5 lightcurve represents the flux of the flare arcade and the background lightcurve is again that of box 10. We use box 4 in place of box 3, however, because box 4 better captures the region that dims in SXRs than does box 3, while box 3 better captures the EUV dimming. Boxes 3 and 4 are separated by about 60″ (both are plotted in Fig. 6b below); this is larger than the uncertainty in the alignment between the SXT and EIT images, which we estimate to be about 10″ based on the co-alignment of features in the other boxes between Figures 2 and 4. Thus the shift in position between the EUV and SXR images for this dimming region may be due to features in the respective lines-of-sight in the two wavebands, or due to evolution of various dynamic flare-associated surrounding features over the time required for visibility in the respective wavebands. Video 2 shows an SXT movie of the same region as video 1.

Figure 6 shows difference images in EUV from EIT (a—c), and in SXRs from SXT (d—f). These are "fixed frame" difference images, in which the same EIT or SXT pre-event

image was subtracted from the subsequent images. In addition, the EIT images are normalized to the image that was subtracted off, that is, these are "percentage difference images" (Wills-Davey & Thompson 1999).

Taken together, Figures 2 through 6 reveal coronal-evolution characteristics of this eruption; in particular they show the intensity variations in the two wavelength regimes as the magnetic field evolves toward eruption, where we take the filament motions to be indicative of the field evolution. While the box 1 feature shows a nearly steady increase in intensity in EUV (Fig. 3b), it shows much more dramatic fluctuations in SXRs (Fig. 5b). Video 2 shows that this feature undergoes several episodes of microflaring, the last of which is occurring in Figure 4b. This microflaring is temporally related to brightening of the loop feature indicated by the arrows in Figure 4b; brightening of this loop is partially captured by the box 4 lightcurves in Figure 5b, between about 7:00 UT and 12:00 UT. After 12:00 UT there is a sharp intensity drop in box 4, coinciding with onset of the main flare in box 5, both of which are close in time to the filament's fast-eruption onset. There are three particularly strong SXR microflares at the box 1 location, and these correlate well with the movement of the filament. Vertical bars in Figures 3a and 5a are at times of the microflare intensity peaks: the earliest peak is near 5:00 UT and corresponds to about the time of the start of the earliest monotonic slow rise of the filament; the second peak is near 8:30 UT and corresponds with a fluctuation in the slow-rise trajectory; and the third peak is near 11:45 UT, which is near the time of the end of the slow rise and the start of the rapid ejection of the filament.

3.3. Dimmings

EUV lightcurves 2 and 3 in Figure 3 and SXR lightcurves 2 and 4 in Figure 5 are from the pair of dimming regions closest to the core eruption region; lightcurve 2 is from the

southern region and lightcurves 3 and 4 are from the northern region. We call these "twin dimmings," and similar dimming pairs are often seen in eruptions (e.g., Sterling & Hudson 1997; Hudson et al. 1999; Zarro et al. 1999; Thompson et al. 1998, 2000; Kahler & Hudson 2001), although more complicated dimmings are also not uncommon (e.g., de Toma et al. 2005). Twin dimmings apparently result when the magnetic field containing a filament or filament channel and the magnetic fields bulging out from this channel leaves the Sun; this field is either a flux rope prior to eruption, or a flux rope forms in the process of erupting. As it lifts off the Sun, the flux rope leaves below it a relatively long and narrow channel of reduced density, and therefore reduced emission. Near the middle of this evacuated channel, however, flare loops rapidly develop, leaving the two end regions as the dimming pair. Figures 2c and 4c show these dimmings best.

Lightcurves from EIT (Fig. 3b) have adequate time cadence to see some details in the evolution of these dimmings. There is a gradual downturn in the intensity beginning at about 07:00 UT in the southern region and 11:00 UT for the northern region. Both locations show an increased rate of dimming from about 12:00 UT, with the maximum dimming occurring at about 13:00 UT. Overall, the southern dimming's decrease roughly tracks the rise of the filament, and the increased rate of intensity decrease in both dimmings coincides closely with the onset of rapid filament rise. At later times there is an upturn in the intensity at both locations due to the intrusion of post-eruption-arcade emission into the dimmed regions. Prior to the onset of either of the twin dimmings, both regions show an increase in intensity, beginning between 4 and 6 UT in the southern region and between 6 and 9 UT in the northern region. In either case, this seems to be due to brightening of isolated loop-like features; it is not certain whether these brightenings are directly related to the subsequent dimmings, which occur over a more extended region than the brightening features alone.

Lightcurves from SXT also show intensity decreases due to these twin dimmings from about 12:00 UT. Details of intensity changes with time, however, are not as easy to determine as with the EUV lightcurves due to the less-regular cadence of SXT compared to EIT.

Remote dimmings and brightenings would be expected to preceed the onset of fast filament eruption if the breakout mechanism is the trigger for the eruption (Moore & Sterling 2006). Lightcurves 6, 7, and 8 in both EUV (Fig. 3b) and SXRs (Fig. 5b) all show dimming at locations that are remote, in the sense that they are farther removed from the erupting filament than are the twin dimmings; more specifically, they are associated with magnetic elements outside the bipolar region that erupts. (Lightcurve 9 is from a location of a set of loops that show changes consistent with temperature variation in a set of loops, see Sterling & Moore (2004a).) After a careful analysis of these dimmings using methods similar to those of Sterling & Moore (2004a), we find that we cannot say whether the primary intensity changes (dimmings and brightenings) or the fast-rise onset begins first, and the data allow that they are concurrent. That is, we cannot determine whether the breakout reconnection was the trigger of, or a consequence of, the eruption. This is similar to our previous findings, as discussed in Moore & Sterling (2006) (also see Williams et al. 2005).

3.4. Magnetic Environment

Figure 7 shows the magnetic environment in the vicinity of the eruption. Overall, at this time the southern hemisphere of the Sun consisted of multiple polarities. We have identified in Figure 7b four alternating-polarity regions that form a quadruple, and from the coronal images from EIT and SXT we suspect that all of these four regions are involved in or affected by the eruption. The filament that erupts resides on a magnetic neutral line

between regions R2 and R3. Figure 7 also shows that the Box 1 region, where microflaring activity prior to eruption occurred, is a location of stronger mixed field, including at least three spot-like negative-field concentrations.

Figure 8 shows in more detail the field concentrations of and around box 1. Flux emerges over about 16 hours. As late as 20:48 UT on Feb 27, box 1 contained no black flux at all, and Figures 8a—8c shows that emergence occurred over the next several hours. Figure 8d shows the unsigned magnetic flux integrated over box 1 as a function of time; this curve is reproduced in Figures 3a and 5a, showing that the largest growth of the flux coincides with the start of the filament's slow rise. We have already pointed out that the SXR microflaring coincides closely with the filament's slow rise, and since the microflares emanate from the location of the growing flux, it is likely that the emerging flux is responsible for both the generation of the microflares and the instigation of the filament's slow rise (see §4).

3.5. CDS Spectra

Figure 9 shows the CDS FOV overlaid onto selected EIT and SXT images. As the northern portion of the filament crossed the CDS FOV, two significant events occur within the CDS FOV. The first is a microflaring of the feature at the location of box 1 in Figures 2 and 4, and the second is the eruption of the northern part of the filament. Arrows in Figures 9a, 9b, and 9d show the microflaring feature; it is in the CDS FOV only in Figure 6a, but Figure 9d shows that there is a bright SXR loop emanating from this microflaring region and extending to the southeast. This is the early flare arcade, also visible in Figure 4c and represented by the lightcurve for box 5 in Figure 5b. This feature becomes visible in SXT images between 12:10 UT and 12:55 UT, and therefore forms after the start of the fast eruption of the filament.

Figures 10a and 10b show CDS O v velocity rasters at times when the box 1 emerging-flux region is in the CDS FOV and when it is undergoing microflaring. From the raster, this microflaring results in motions along or near the magnetic field traced by the bright SXR loop emanating from the this region in Figure 9d. Figure 9b also overlays onto the CDS raster of Figure 10a the magnetogram of Figure 8a. This overlay shows that the microflaring feature occurs at the location of the newly-emerged flux concentration, and this match supports our conclusion that the emerging flux was responsible for the microflare.

Figures 10c through 10f show the panels where motions associated with the erupting filament are clearly apparent in CDS. At times just prior to these, from 12:01 UT to 12:23 UT, it is barely possible for us to pick out the filament in the velocity movies, indicating filament velocities < 20 km s^{-1}, which is the approximate noise level of the velocity images. Figure 3a shows that there may be subtle motions (of magnitude similar to the error bars) in this northern portion of the filament projected on the solar disk from about 08:00 UT. From Figure 10, the filament has Earthward-directed velocities of up to a few tens km s^{-1} from about 12:23 UT, reaching 100 km s^{-1} or more from around 12:44 UT. Since the lowest detectable CDS velocities are around 20 km s^{-1}, we cannot resolve possible slow-rise filament motions of this portion of the filament, which are likely to be much smaller than 20 km s^{-1} based on our estimates in §3.1 for the velocities of the southern portion of the filament. Figures 10d—10f do tell us, however, that between 12:34 UT and about 13:00 UT the northern portion of the filament does have a line-of-sight velocity comparable to our estimated velocity of about 45 km s^{-1} for the southern portion of the filament at similar times.

4. Implications for the Slow Rise Mechanism, and for the Fast-Rise-Onset Mechanism

First we consider what may have driven the slow-rise of the filament. A strong hint comes from the activity around the box 1 location in Figures 2 and 4. Figure 8 shows that there is flux emergence at this location, and Figures 3a and 5a show that the emergence coincides approximately with the filament's slow rise and the start of the SXR microflaring.

Figure 11 shows our interpretation of these events, in the immediate vicinity of the filament eruption. Emerging flux of box 1 interacts with the pre-existing magnetic arcade that arches over and ties down the overlying filament field, and "tether-weakening" reconnection occurs between these two flux systems. In contrast to "tether-cutting" reconnection, which reduces the filament field's connection to the photosphere and builds a flux rope, tether-weakening reconnection, in the present setup, results in longer, higher-arching loops in the overlying arcade (Moore & Roumeliotis 1992). This reconnection heats the plasma on the reconnected field lines, producing the fan-like SXR structure together with the SXR microflare brightenings. As the reconnection progresses the fan field expands, allowing the filament-carrying field to expand, and the filament rises slowly in step with the fan-field expansion.

As box 1 is spatially separated from the location where we measure the strongest filament motion (southern fiducial of Fig. 2a), we must consider how long it would take for a microflare disturbance generated by an emerging magnetic element of box 1 to be transmitted to our measurement point on the filament. From Figure 2a this distance is of order $300''$, or about 2×10^5 km. We measured the average magnetic field strength of the region around the filament (spanning heliocentric longitude $0''$ to $200''$, and latitude $-400''$ to $0''$; see Fig. 2b) to be 12 G. Taking $\rho \sim 10^{-15}$ g cm^{-3} to represent a quiet-region loop density (e.g., Priest 1982, Table 6.2) gives an Alfvén velocity of $v_A = B/(4\pi\rho)^{1/2} \sim 1000$ km s^{-1},

with a corresponding Alfvén travel time of about 3.5 min between the emerging flux and the filament-measurement location. Given the roughness of our estimates and the poor cadence of the SXT images (resulting in poor cadence for the SXR microflare curve in Fig. 5), this travel time is consistent with the changes in filament motion occurring in response to the SXR microflares.

Eventually, the slow rise switches to fast rise as the filament erupts, producing the CME and strong flare heating. But as in our previous studies (Moore & Sterling 2006), we are not able to determine the exact mechanism for the onset of this transition from slow to fast rise. A possibility for our event is that continued tether-weakening reconnection could result in the overall system evolving to an unstable state, resulting in the fast eruption. In fact, the third and final SXR microflare could be due to the tether-weakening reconnection episode that finally allows the system to "fall off the table" and become explosively unstable. If instead, tether cutting is the mechanism triggering fast eruption, then we would expect a brightening increase at the location of box 5 at the time of the onset of the filament's fast rise. From Figure 5, the time of flare brightening and fast filament rise onset are very close, but it is not possible to make a definitive conclusion of whether the brightening begins early enough to be consistent with a tether cutting mechanism. Similarly, as discussed in §3.3, from our data we also cannot determine whether breakout was the trigger of the fast-rise onset for this event.

5. Summary and Discussion

We observed a large-scale ($\approx$ 300,000 km) filament that erupted from a quiet solar region, and the filament and associated ejected fields produced a CME. By following the motions of the filament we can infer how the otherwise-invisible enveloping field structures evolve toward eruption. The earliest motion that we can detect of the filament

is a nearly-constant slow rise of about 1 km s^{-1} projected against the disk, which we estimate to be about 5 km s^{-1} in the vertical direction. After about 6 hours the filament undergoes acceleration and erupts from the Sun, leaving a post-flare arcade in its wake. Weak-intensity dimmings began near the filament during the slow-rise phase, and these dimmings became pronounced twin dimmings at the time of eruption. Dimmings also occur at more remote locations, which could be indicative of breakout-type reconnection. New magnetic flux emerges adjacent to the filament over a 15 hour period that includes the slow-rise and eruption of the filament, with the fastest rate of emergence coinciding with the onset of the slow rise. Several SXR microflares occur at the location of emergence, and the three strongest ones peak respectively near the times of filament slow-rise onset, a kink in the slow-rise trajectory, and the time of transition from slow rise to fast eruption of the filament. Spectra from CDS of the first microflare show that it has rapid jet-like upflows. These spectra also show that the northern portion of the filament erupts with velocities similar to that of the southern portion of the filament, a fact that we could not obtain without the spectra since the northern part of the filament erupts nearly directly along the Earth-Sun line-of-sight.

The coronal hole in the vicinity of the filament (see Figs. 4 and 6) undergoes intensity changes during eruption, and it could have some implication in the large scale evolution of the magnetic system involving the filament. In Figure 12 we present such a possibility (described in the caption), including a modified breakout-type scenario similar to that of Sterling et al. (2001). Our interpretation of these events and our 2D cartoon sketches, however, are speculative and necessarily simplistic, and a full understanding of the observations would require non-linear force-free 3D MHD modeling.

It has long been known that localized newly-emerging flux frequently plays an important role in the onset of solar eruptions (e.g., Rust 1976; Moore et al. 1984; Parker

1987), and this has resulted in emerging-flux-based theoretical models since at least Heyvaerts, Priest, & Rust (1977). Wang et al. (2004) have observed rapid flux emergence near the time and place of flare onset, although their event was not associated with a filament eruption. SXR microflares have also been seen in association with emerging flux (Tang et al. 2000; Shimizu et al. 2002). Also, Feynman & Ruzmaikin (2004) found an association between emerging flux and the onset of the slow rise in a filament; our work supports their findings, and we give new evidence that the agent by which the emerging flux leads to the slow rise is tether-weakening reconnection.

Our strongest evidence for tether-weakening reconnection causing the slow rise of the filament field (which is part of a more general eruption field) is the bright SXR fan structure stemming from the SXR microflares, the connection of these with the emerging flux, and their coordination with the filament trajectory. Both the fan and the microflares, however, are prominent only in SXRs, not EUV. Previous filament slow-rise studies may have missed signatures for tether weakening because they generally either did not include SXRs, or used SXT SXR images of insufficient cadence. An active-region filament eruption studied by Sterling & Moore (2005) also showed a connection between localized EUV and SXR brightenings, recently-emerged flux, and the slow-rise phase of a filament, although the data quality were not sufficient to conclude whether tether weakening was operating in that case. Similarly, Williams et al. (2005) present another observational example of possible tether weakening due to the intrusion of localized newly-emerging flux into a magnetically-stressed region; they did not see brightening by the inferred reconnection however, probably because they observed in EUV without SXRs. Schmieder et al. (2000) also present an example of an X-ray bright point in spatial and temporal proximity to a destabilized filament, which they suggested could be related to emerging flux. These additional examples suggest that tether weakening causes the slow-rise phase of erupting filaments in at least a class of events. It still remains to be seen, however, whether tether weakening by localized emerging flux,

leading to a CME explosion, is rare or common. In addition, more observations are needed to determine what triggers the fast eruption.

REFERENCES

Antiochos, S. K. 1998, ApJ, 502, L181

Antiochos, S. K., DeVore, C. R., & Klimchuk, J. A. 1999, ApJ, 510, 485

Anzer, U., & Heinzel, P. 2005, ApJ, 622, 714

Bong, S.-C., Moon, Y.-J., Cho, K.-S., Kim, Y.-H., Park, Y. D., & Choe, G. S. 2006, ApJ, 636, 169

Brueckner, G. E., et al. 1995, Sol. Phys., 162, 357

Canfield, R. C., Hudson, H. S., & McKenzie, D. E. 1999, Geophys. Res. Lett., 26, 627

Chen, P. & Shibata, K. 2000, ApJ, 545, 524

Delaboudinière, J.-P. et al. 1995, Sol. Phys., 162, 291

de Toma, G., Holzer, T. E., Burkepile, J. T. & Gilbert, H. R. 2005, ApJ, 621, 1109

Engvold, O., Jakobsson, H., Tandberg-Hanssen, E., Gurman, J. B., & Moses, D. 2001, Sol. Phys., 202, 293

Fan, Y., & Gibson, S. E. 2004, ApJ, 609, 1123

Feynman, J., & Ruzmaikin, A. 2004, Sol. Phys., 219, 301

Forbes, T. G., & Isenberg, P. A. 1991, ApJ, 373, 294

Forbes, T. G. 2000, J. Geophys. Res., 105, 23,153

Gary, G. A. & Moore, R. L. 2004, ApJ, 611, 545

Gibson, S. E., & Fan, Y. 2006, J. Geophys. Res., 111, A12,103

Harrison, R. A., et al. 1995, Sol. Phys., 162, 233

Heyvaerts, J., Priest, E., & Rust, D. M. 1977, Sol. Phys., 53, 255

Hudson, H. S., Acton, L. W., Harvey, K. L., & McKenzie, D. E. 1999, ApJ, 513, L83

Kahler, S. W., Moore, R. L., Kane, S. R., & Zirin, H. 1988, Sol. Phys., 328, 824

Kahler, S. W., & Hudson, H. S. 2001, J. Geophys. Res., 106, 29239

Klimchuk, J. A. 2001, in: Space Weather, Geophysical Monograph, 125, 143

Lin, J., Forbes, T. G., Isenberg, P. A., & Démoulin, P. 1998, ApJ, 504, 1006

Lin, J., Soon, W., & Baliunas, S. L. 2003, New Astron. Reviews, 47, 53

Linker, J., Lionello, R. Mikic, Z., & Amari, T. 2001, J. Geophys. Res., 106, 25,165

Mein, N., Schmieder, B., DeLuca, E. E., Heinzel, P., Mein, P., Malherbe, J.-M., & Staiger, J. 2001, ApJ, 556, 438

Moore, R. L., and LaBonte, B. 1980, in Proc. Symp. on Solar and Interplanetary Dynamics, Reidel, Boston, 207

Moore, R. L., & Roumeliotis, G. 1992, in Eruptive Solar Flares, ed. Z. Svestka, B. V. Jackson, & M. E. Machado (Berlin: Springer), 69

Moore, R. L., Sterling, A. C., Hudson, H. S., & Lemen, J. R. 2001, 552, 833

Moore, R. L., Hurford, G. J., Hones, H. P, & Kane, S. R. 1984, ApJ, 276, 379

Moore, R. L. & Sterling, A. C. 2006, in Solar Eruptions and Energetic Particles (N. Gopalswamy, ed.), (AGU, Washington, D.C.), in press

Parker, E. N. 1987, ApJ, 312, 868

Priest, E. R. 1982, Solar Magnetohydrodynamics (Dordrect: Reidel)

Rust, D. M. 1976, Sol. Phys., 47, 21

Rust, D. M. & LaBonte, B. J. 2005, ApJ, 622, L69

Scherrer, P. H., et al. 1995, Sol. Phys., 162, 129

Schmieder, B., Delannée, C., Yong, D. Y., Vial, J. C., & Madjarska, M. 2000, A&A, 358,
      728

Schmieder, B., Lin, Y., Heinzel, P., & Schwartz, P. 2004, Sol. Phys., 221, 297

Shimizu, T., Shine, R. A., Title, A. M., Tarbell, T. D., & Frank, Z. 2002, ApJ, 574, 1074

Sterling, A. C., & Hudson, H. S. 1997, ApJ, 491, L55

Sterling, A. C., & Moore, R. L. 2001, J. Geophys. Res., 106, 25227

Sterling, A. C., & Moore, R. L. 2003, ApJ, 599, 1418

Sterling, A. C., & Moore, R. L. 2004a, ApJ, 602, 1024

Sterling, A. C., & Moore, R. L. 2004b, ApJ, 613, 1221

Sterling, A. C., & Moore, R. L. 2005, ApJ, 630, 1148

Sturrock, P. A. 1989, Solar Phys., 121, 387

Sturrock, P. A., Weber, M., Wheatland, M. S., & Wolfson, R. 2001, ApJ, 548, 492

Tandberg-Hanssen, E., Martin, S. F., & Hansen, R. T. 1980, Sol. Phys., 65, 357

Tang, Y. H., Li, Y. N., Fang, C., Aulanier, G., Schmieder, B., Démoulin, P., & Sakurai,
      T. 2000, ApJ, 534, 482

Tsuneta, S., et al. 1991, Sol. Phys., 136, 37

Thompson, B. J., Plunkett, S. P., Gurman, J. B., Newmark, J. S., St. Cyr, O. C., & Michels, D .J. 1998, Geophys. Res. Lett., 25, 2465

Thompson, B. J., Cliver, E. W., Nitta, N., Delannée, C., & Delaboudinière, J. P. 2000, Geophys. Res. Lett., 27, 1431

Wang, H., et al. 2004, ApJ, 605, 931

Wiik, J. E., Schmieder, B., Kucera, T.,Poland, A., Brekke, P, & Simnett, G. 1997, Sol. Phys., 175, 411

Williams, D. R., Török, T., Démoulin, P., van Driel-Gesztelyi, L., & Kliem, B. 2005, ApJ, 628, L163

Wills-Davey, M. J., & Thompson, B. J. 1999, Sol. Phys., 190, 467

Yashiro, S., Gopalswamy, N., Michalek, G., St. Cyr., O. C., Plunkett, S. P., Rich, N. B., & Howard, R. A. 2004, JGR, 109, A06109

Zarro, D. M., Sterling, A. C., Thompson, B. J., Hudson, H. S., & Nitta, N. 1999, , 520, L139

Fig. 1.— LASCO difference image at 16:50 UT from the C2 coronagraph, showing the halo CME resulting from the filament eruption of this paper. The insert is an EIT difference image from 16:48 UT. This image is from the LASCO online catalog (Yashiro et al. 2004).

Fig. 2.— EUV images of the erupting region from EIT, taken with its 195Å filter. Arrows in (a) and (b) point to the filament, which is starting to erupt in (b), and has erupted and by the time of panel (c), and therefore the filament is not visible in (c) or (d). The nearly horizontal lines in (a) are fiducials along which the height of the filament projected on the disk is measured in Figs. 3a and 5a. Boxes, labeled in (d), are regions for which lightcurves are generated in Fig. 3b. North is up and west is to the right here and in all solar images in this paper. The EIT images in these panels are frames from Video 1.

Fig. 3.— (a) Trajectory of the filament as a function of time along fiducials of Fig. 2a, with the bottom (top) trajectory from the southern (northern) fiducial. Initial heights are arbitrarily set at approximately 0 km and 10,000 km, and motion upward (downward) reflects motions projected on the disk toward the west (east). Error bars are 1σ uncertainties based on three independent measurements of the filament motion. The curve labeled "B flux" is from Fig. 8 and discussed further below. Vertical bars show times of the peaks of SXR microflare bursts in Fig. 5. (b) Lightcurves from correspondingly-numbered boxed regions in Fig. 2. Curve 10 is from a region showing little change and represents background variations. Different line thicknesses, and dashed and solid lines, are for clarity only, and all plots are shifted arbitrarily on the vertical axis for clarity.

Fig. 4.— Similar to Fig. 2, but from soft X-ray (SXR) images from SXT, taken with its AlMg filter. Boxes, labeled in (d), are regions for which lightcurves are generated in Fig. 5b. Box 5 is omitted from panel (a) to show the central features more clearly. Arrows in (b) point to a loop that brightens in SXRs near the start of the filament's fast-rise phase. A coronal hole is visible in the NE of the frames, east of -450 in the abscissa, and between

approximately -200 and +400 in the ordinate. The SXT images in these panels are frames from Video 2.

Fig. 5.— (a) Same as in Fig. 3a, but with the filament trajectory plotted on a logarithmic scale; error bars are given in Fig. 3a but omitted here for clarity. The curve labeled "B flux" is from Fig. 8 and discussed below. (b) Lightcurves from correspondingly-numbered boxed regions in Fig. 4. Curve 10 is from a region showing little change and represents background variations. Curve 2 has been magnified by a factor of 5 to show better its variations. Different line thicknesses, and dashed and solid lines, are for clarity only, and all plots are shifted arbitrarily on the vertical axis for clarity. Stars on curve 10 are plotted at times of SXT images, showing the cadence of the observations. In (a), vertical bars show times of the peaks of SXR microflare bursts from the box 1 lightcurve of (b).

Fig. 6.— Fixed-frame intensity difference images of the erupting region, all from 2001 February 28. Panels (a)—(c) are percentage difference images from EIT, with the image used in forming the percentage difference from 06:00 UT. Panels (d)—(f) are SXT difference images, with the subtracted image from 06:36 UT. Arrows in (e) point out a ridge next to a coronal hole that brightens in SXT images, and dims in both EIT (c) and SXT (f) images.

Fig. 7.— Magnetic setting in the vicinity of the eruption. (a) MDI magnetogram at the time indicated in the heading. (b) Same as (a), but with red and blue contours representing positive and negative flux regions, respectively. Labels R1—R4 denote alternating positive and negative regions that form a quadrupole involved in the eruption. (c) Magnetogram contours of (b) overlaid on an EIT image prior to eruption. (d) Magnetogram contours of (b) overlaid on an SXT image from after the eruption. Contour levels are 25, 40, and 300 G. Boxes in (b—d) are those of Figs. 2 and 4.

Fig. 8.— Close-up of the magnetic region around box 1. Panels (a)—(c) show MDI magne-

tograms at three different times, where the black rectangle is the same as box 1 in Figs. 2 and 4. Panel (d) shows the unsigned total magnetic flux in box 1; this curve is also plotted in Figs. 3a and 5a.

Fig. 9.— Field-of-view (FOV) of CDS (rectangle box) overlaid onto (a—c) EIT images and (d) an SXT image; since CDS was pointing at the same fixed heliocentric location (i.e., CDS was not tracking solar rotation) the solar images rotate with respect to the CDS FOV over time. Arrows in (a), (b), and (d) indicate a location showing microflaring during the pre-eruption phase; this is at the location of box 1 in Figs. 2 and 4 and is in the CDS FOV in (a).

Fig. 10.— CDS O v velocity rasters (a) when a microflare is occurring (indicated by the arrow) at the location of box 1 in Figs. 2 and 4 and at the location indicated by the arrows in Figs. (9a), (9b), and (9d). Panel (b) is the same as (a) with the MDI magnetogram of 2001 Feb 28, 01:35 UT overlaid, with contours the same level as those in Fig. 7. Panels (c—f) show the filament when it is most visible in the velocity diagrams. Prior to the time of (a), it is barely detectable, with velocities near the noise level (about -20 km s^{-1}) in movies constructed from the CDS velocity rasters. Negative values indicate blue-shifted motions. Values in (f) have higher uncertainties (and are likely stronger than they appear), since the signal is weak and therefore the profiles cannot be fit as well.

Fig. 11.— Schematic drawings of the erupting region in the vicinity of the filament during the slow-rise phase. (a) 3D view, with black dashed line representing the magnetic neutral line, black wavy line the filament, arched blue lines the magnetic field prior to a tether-weakening-reconnection episode, and adjacent red lines the same field slightly displaced by the reconnection episode; the red cross shows the location of the reconnection. These red field lines form a fan-like structure that arches over the filament, and is illuminated in SXRs. (b) A cross-sectional cut of (a) at the position of the emerging flux. Blue and red lines are

the same as in (a), and the filament is in the dip of a twisted field line; the tether-weakening reconnection lengthens field lines of the confining arcade, allowing the sheared core field to expand upward, resulting in the filament's slow rise.
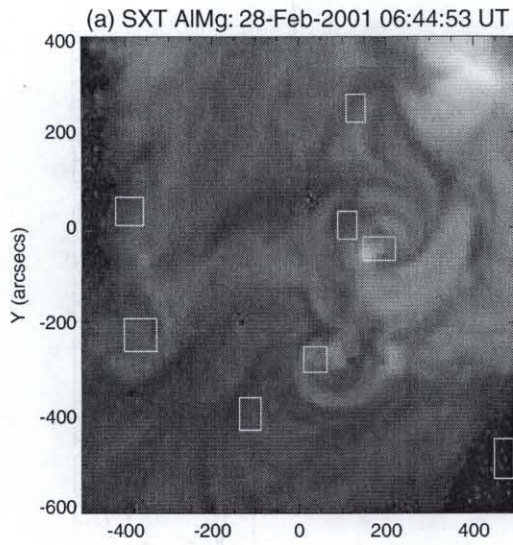
Fig. 12.— Schematic drawings of the larger-scale region, illustrating possible interactions between the erupting field and the coronal hole noted in Figs. 4 and 6. Panel (a) shows the set up near the time of the start of filament's slow rise. The bipole associated with the emerging flux is adjacent to R3, and the blue field line above it is one of the loops arching over the filament in Fig. 11a. Still-higher-altitude black loops are oriented so that reconnection with open coronal hole fields emanating from R1 is possible at the location of the red X. In (b), reconnection between these fields has started, with the reconnection-product fields dashed. The new loops formed between R1 and R2 lead to the remote SXT brightening of Fig. 6e, and to a reduction of the coronal hole. Meanwhile, the filament-arcade blue field continues to expand upward. In (c) the erupting filament-arcade blue field has "broken out" through the external reconnection site and the legs of the erupting blue field internally reconnect at the location of the red X, causing the main flare and unleashing the CME flux rope plasmoid. After the CME plasmoid pinches off and escapes, the most-recently-created R1— R2 loop will reconnect with the most-recently-created open field (both dashed). In (d) the dashed field lines of (c) have reconnected to produce new dashed reconnection-product fields (dashed here), and a new set of fields are coming together and will reconnect. Eventually, the entire system relaxes via these reconnections until a state similar to panel (a) is re-instated, although in this final state the R2—R3 arcade is more relaxed and less inflated than that of panel (a) because the eruption has occurred. This could result in the dimming apparent in Fig. 6f.
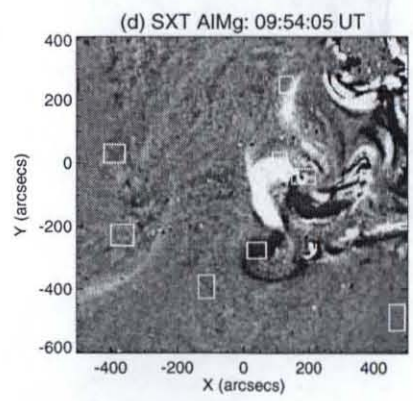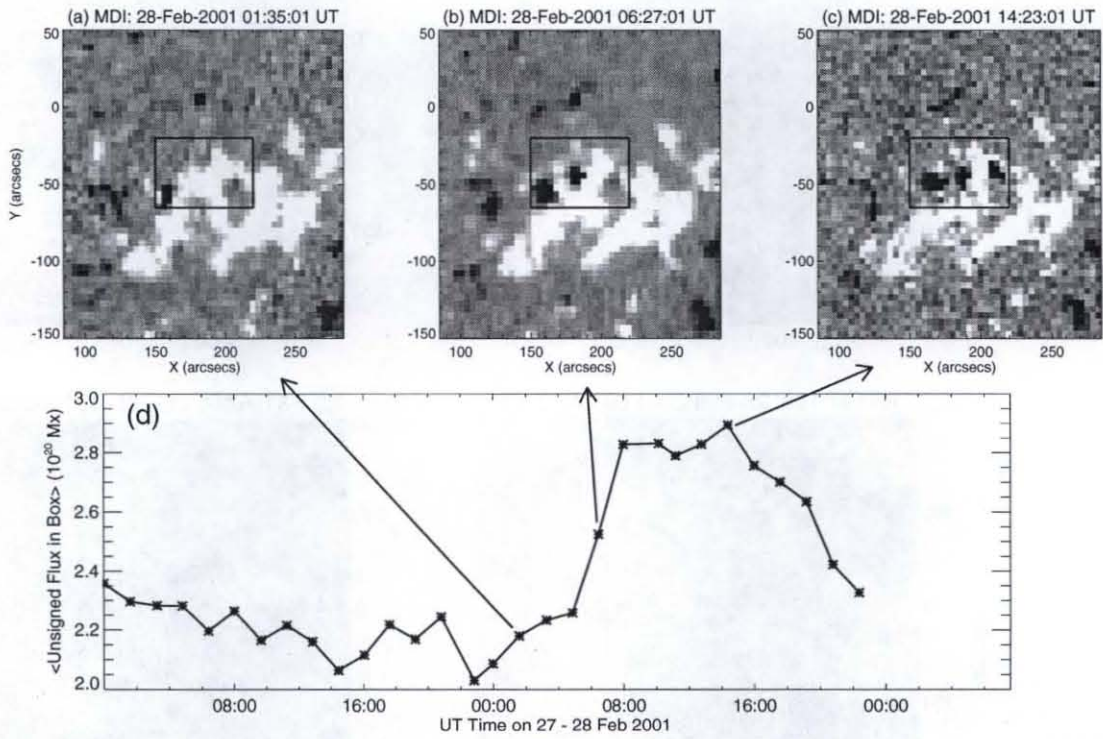
f1.eps

(a) EIT 195: 28-Feb-2001 00:48:07 UT
(b) EIT 195: 28-Feb-2001 12:35:35 UT
(c) EIT 195: 28-Feb-2001 14:35:22 UT
(d) EIT 195: 28-Feb-2001 19:35:23 UT

f2.eps

f3.eps

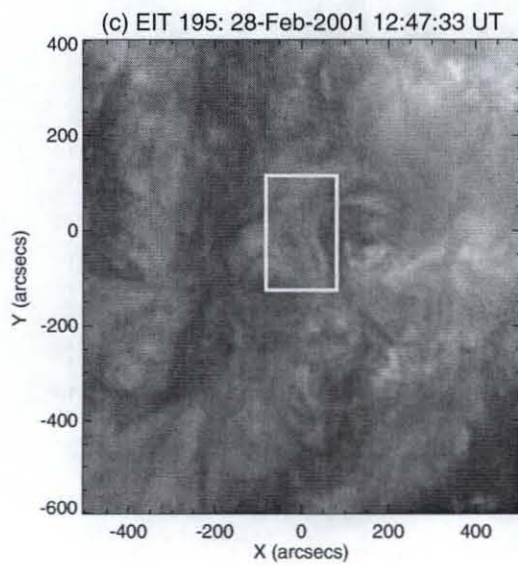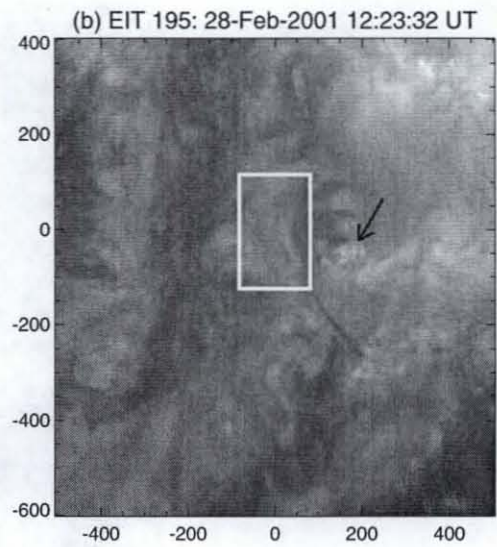(a) SXT AlMg: 28-Feb-2001 06:44:53 UT
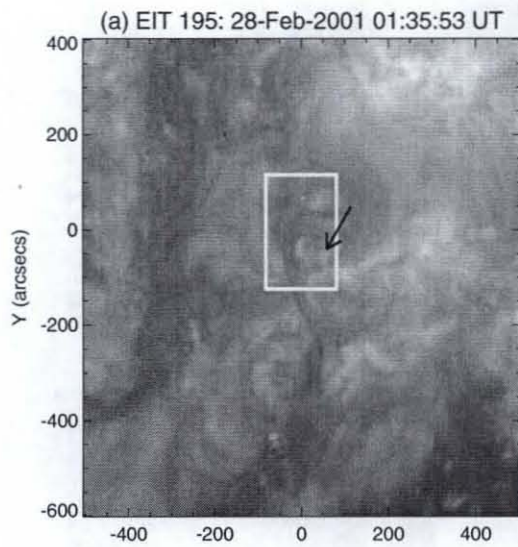
(b) SXT AlMg: 28-Feb-2001 11:40:19 UT

(c) SXT AlMg: 28-Feb-2001 13:03:31 UT

(d) SXT AlMg: 28-Feb-2001 16:05:23 UT

f4.eps

f5.eps

(a) EIT 195: 09:59:27 UT (b) EIT 195: 13:24:49 UT (c) EIT 195: 15:59:25 UT
(d) SXT AlMg: 09:54:05 UT (e) SXT AlMg: 13:24:51 UT (f) SXT AlMg: 16:05:23 UT

f6.eps

(a) MDI: 28-Feb-2001 12:47:01 UT
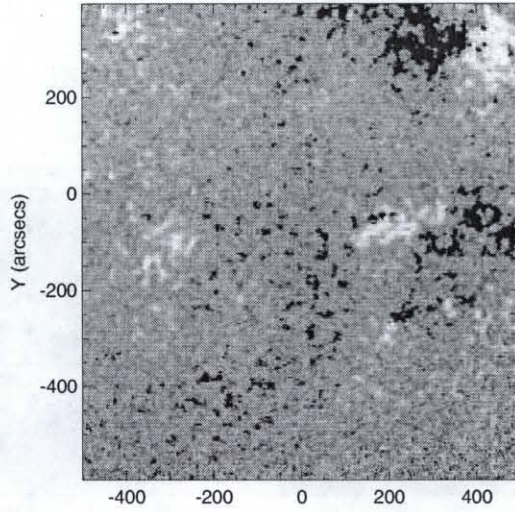
(b) MDI: 28-Feb-2001 12:47:01 UT
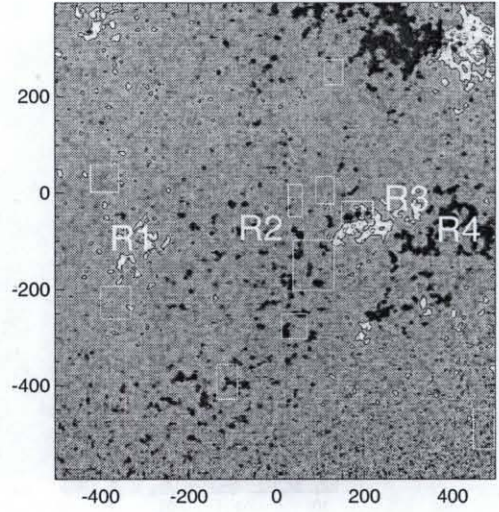
(c) EIT 195: 28-Feb-2001 09:11:22 UT

(d) SXT AlMg: 28-Feb-2001 13:03:31 UT

f7.eps

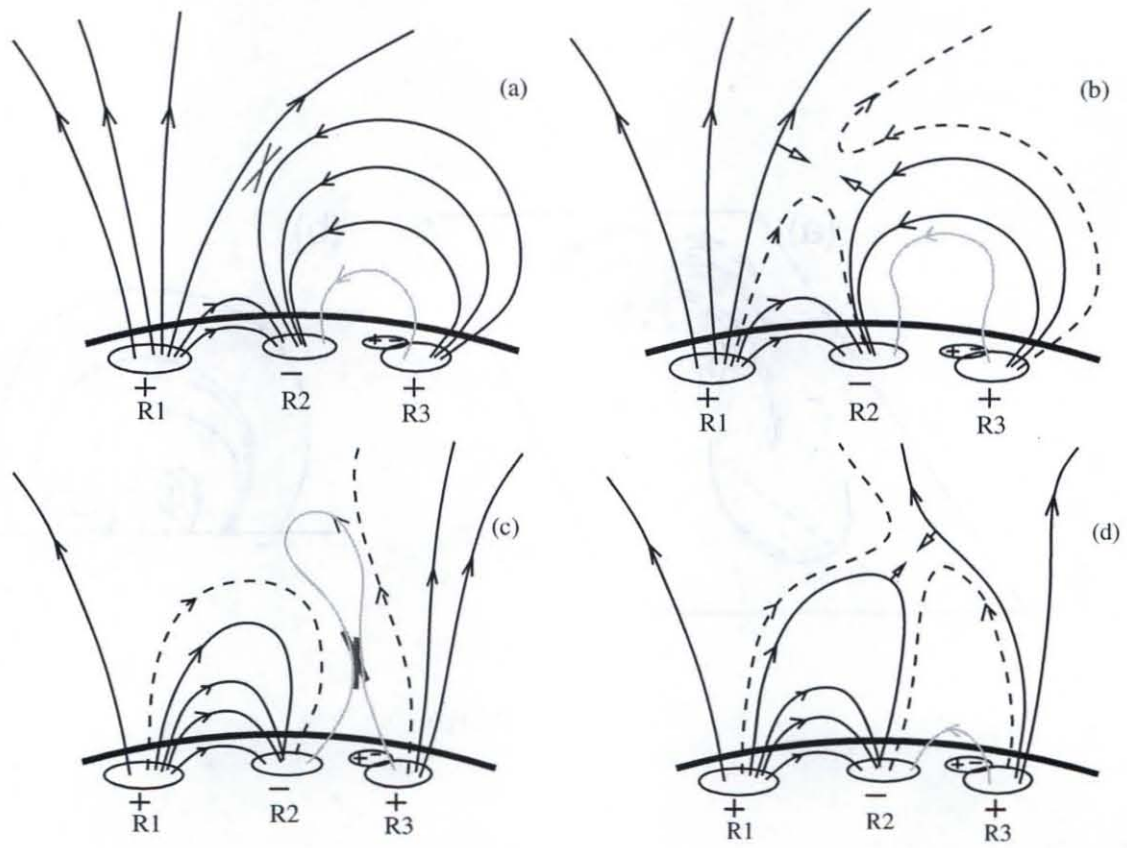(a) MDI: 28-Feb-2001 01:35:01 UT   (b) MDI: 28-Feb-2001 06:27:01 UT   (c) MDI: 28-Feb-2001 14:23:01 UT

(d)

f8.eps

(a) EIT 195: 28-Feb-2001 01:35:53 UT

(b) EIT 195: 28-Feb-2001 12:23:32 UT

(c) EIT 195: 28-Feb-2001 12:47:33 UT

(d) SXT AlMg: 28-Feb-2001 12:54:59 UT

f9.eps

f10.eps

(a)

(b)

f11.eps

(a)

(b)

(c)

(d)

R1 R2 R3

f12.eps